Supplementary Information

Atomically engineered interfaces yield extraordinary electrostriction

Haiwu Zhang[1*], Nini Pryds[1*], Daesung Park[2], Nicolas Gauquelin[3], Simone Santucci[1], Dennis V. Christensen[1], Daen Jannis[3], Dmitry Chezganov[3], Rata Diana[4], Ivano E. Castelli[1], Johan Verbeeck[3], Igor Lubomirsky[5], Dragan Damjanovic[2], and Vincenzo Esposito[1*]

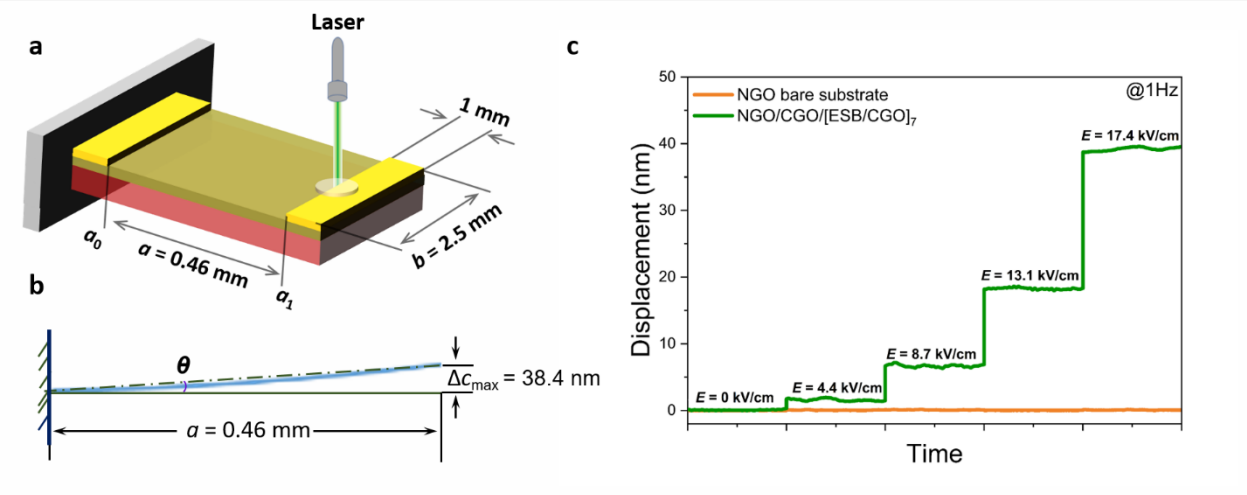

Supplymentary Fig. 1 | Electrostrictive measurement. **a**. Schematic illustration of the cantilever's geometry. The displacement along the out-of-plane direction is measured as a function of time under an electric field. **b**. Schematic illustration of the deformation of the cantilever. The blue line denotes the curvature. **c**. A comparison of the displacements of bare NGO$_{(100)}$ substrate with NGO/CGO/[ESB/CGO]$_N$ as a function of electric field using the planar electrode configuration.

Extended Data Fig. 1a schematically illustrates the geometry of the cantilever with planar electrode configuration. The displacements (Δc) that respond to the electric field at the free end of the cantilever (a_1) are measured. This configuration yields the longitudinal electrostriction coefficient (*i.e.* M_{13}). The distance (a) between the two electrodes is 0.46 mm, the width (y) is 2.5 mm, and the thickness of the NGO substrate is 0.1 mm.

The induced curvature (Δk) is calculated by $\Delta k = 2\Delta c/(a^2)$.[33] The in-plane stress is then calculated using the well-known Stoney formula[34]

$$\Delta\sigma = \frac{Y_{sub}}{1-v_{sub}}\frac{t_{sub}^2}{6t_{film}}\Delta k \qquad 1$$

where Y_{sub} is Young's modulus, v_{sub} is the Poisson ratio, t_{sub} and t_{film} are the thickness of the substrate and film, respectively.

Then M_{xx} is obtained by linear fitting the stress against electric field squared by

$$M_{xx} = \frac{\Delta\sigma}{E^2 \cdot Y_{film}} \quad (2)$$

where Y_{film} is Young's modulus of the heterostructures, which is taken to be a weighted average of CGO and ESB. The Yongs's modulus(Poisson ration) for NGO, CGO and ESB are 200.97(0.29)[35], 200(0.33)[36], and 72.8(0.39)[37], respectively.

To account for the electric field distribution, we performed finite element modelling (FEM) following the procedure described by Nigon *et al*.[29] Here, the electric field distribution was calculated using a 2D model of the cantilever geometry in Fig. 1. A grounded electrode and a biased electrode were placed on top of the thin film deposited on the NGO substrate. The cantilever was further surrounded by air on the top and bottom. The deposited superlattice is modelled as a single dielectric layer. A custom mesh was created to account for the high aspect ratio of the thin film. The average electric field in the thin film was found to be invariant to its thickness in the probed range ($38 \leq t_{film} \leq 80$ nm). The electric field distribution is displayed in Fig. 2a where it is observed that E_x is the dominating component in the film, consistent with previous studies.[29, 38] The electric field is found to be fairly constant in the majority of the electrostrictor ($E_x = 0$ below the electrodes and $E_x \sim V/a$ between the electrodes) with only significant inhomogeneities occurring close to the edge of the electrodes where E_x increases from 0 below the electrodes, encounters a peak and decreases to a constant value. The average of E_x and E_x^2 is displayed in Fig. 2b as a function of the dielectric constant of the electrostrictor. For all probed dielectric constants, the average of E_x can be well approximated by $E_x \approx V/a$. However, for low values of the dielectric constants, the peak in E_x close to the electrode edge increases, leading to an increasing average of E_x^2. However, the thinner the film with respect to the electrode distance, the less the impact of the region close to the electrode. The geometry and high dielectric constant of the electrostrictive

heterostructure used here ensure that $E_x \approx V/a$ and $E_x^2 \approx (V/a)^2$ are fair approximations, and these will be used in the following for convenience.

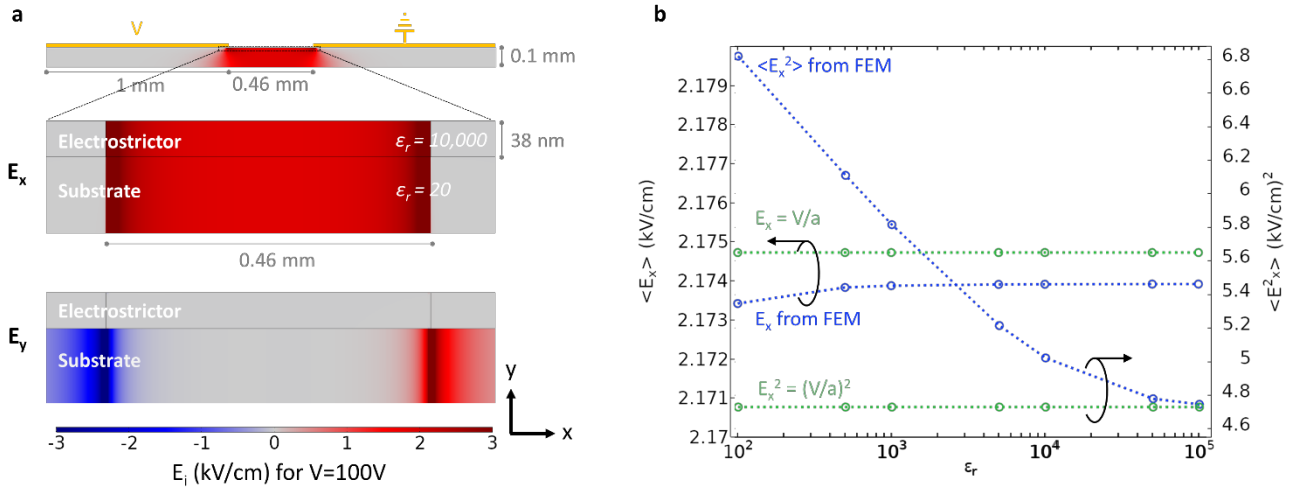

Supplymentary Fig. 2 | Electric field distribution by finit element simulations. a. Distribution of the x- and y-component of the electric field (E_x and E_y) in the electrostrictive cantilever and NGO substrate when an electrostatic potential of V = 100V is applied. **b** The average of the electric field and squared electric field as a function of the dielectric constant of the thin film. The average is calculated in the 0.46 mm x 38 nm region of the electrostrictive film between the electrodes and compared to the naïve prediction where $E_x = V/a$. Note that the dielectric displacement field is channelled by the high dielectric constant materials, i.e., CGO.

For NGO/CGO/[ESB/CGO]$_7$, the maximum displacement is 38.4 nm under the highest electric field (V/a = 17.4 kV/cm) at 1Hz. This gives a deformation of $\Delta c_{max}/a$ = 38.4 nm/0.46 mm = 8.35×10^{-5} << 1% (Fig. 1b), corresponding to an angle change of 0.00478295 °. Such a small angle change indicates that the 'bending' of the cantilever can be neglected. Fig. 1b further show the displacements of bare NGO$_{(100)}$ substrate with planar electrode configuration. It is clear that NGO is not electrostrictive active. Thus the contributions associated with a high electric field, such as polarization or electrostatic force (*i.e.* Maxwell stress tensor), can be neglected. This assumption is consistent with the results shown in Fig. 1c in the main text: with the same planar electrode configuration, M_{xx} increases by approximately two orders of magnitude from NGO/CGO to NGO/CGO/[ESB/CGO]$_7$ (Fig. 1c, main text), demonstrating that the variation of the thin film is dominating the electromechanical response.

a

M-O^{2-}	*A*/eV	*ρ*/Å	*C*/eV Å^6	ref
Ce^{4+}-O^{2-}	1809.68	0.3547	20.40	39
Gd^{3+}-O^{2-}	1885.75	0.3399	20.34	39
Bi^{3+}-O^{2-}	2496.91	0.3305	18.25	This work
Er^{3+}-O^{2-}	1719.91	0.3389	17.55	40
O^{2-}-O^{2-}	9547.96	0.2192	32.0	39, 40

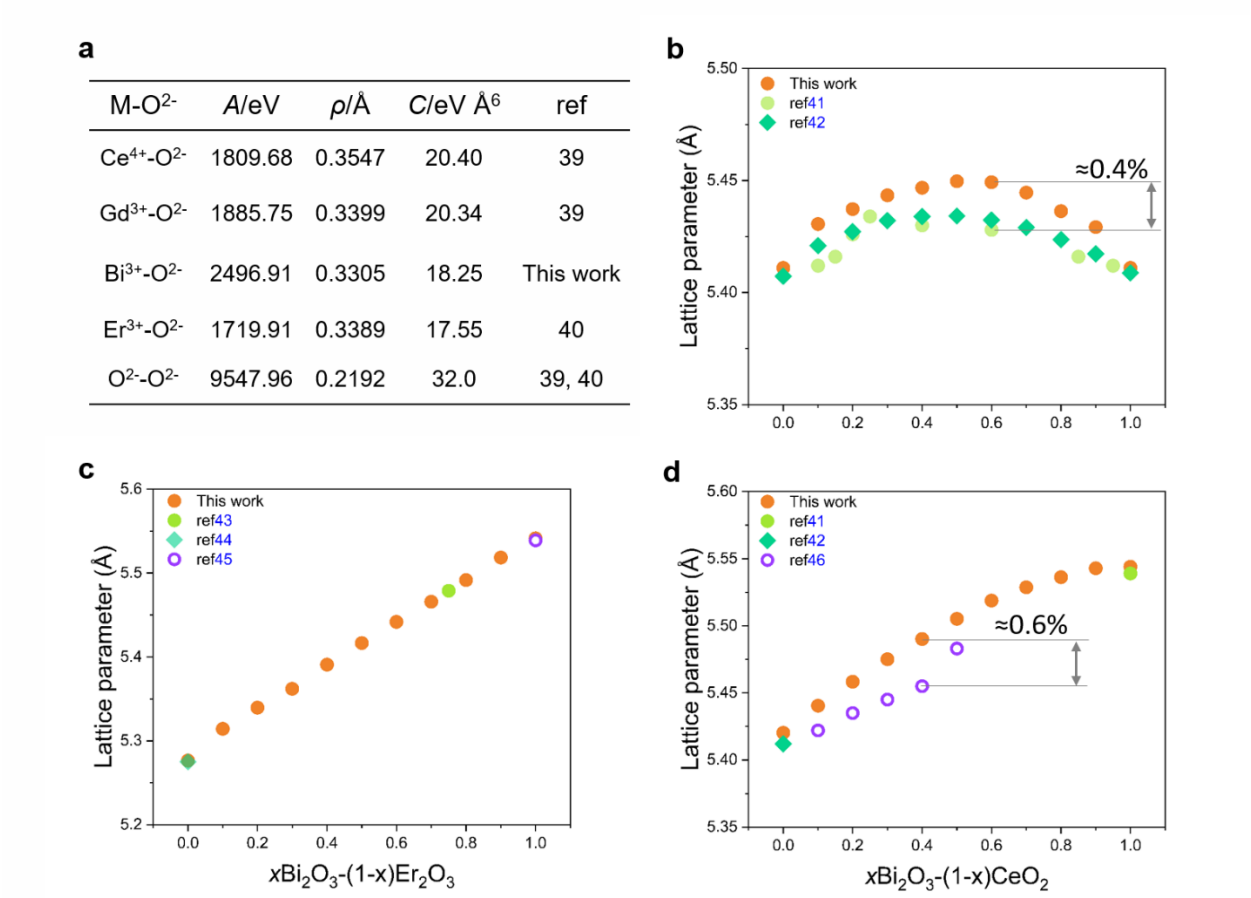

Supplymentary Fig. 3 | Atomic scale simulations. **a**. Table showing the short-range Buckingham potential parameters. **b**, **c** and **d** comparison of calculated and experimental lattice parameters for xGd_2O_3-(1-x)CeO_2. (**b**), xEr_2O_3-(1-x)Bi_2O_3 (**c**), and xBi_2O_3-(1-x)CeO_2 (**d**). The maximum difference between the calculated values and experimental values is ~0.4% xGd_2O_3-(1-x)CeO_2 and ~0.6% for xBi_2O_3-(1-x)CeO_2. The lattice parameters for xGd_2O_3-(1-x)CeO_2 were taken from ref 41 and 42. The lattice parameters for Bi_2O_3, Er_2O_3 and $Er_{0.8}Bi_{1.2}O_3$ were taken from ref 43, 44 and 45, respectively. The lattice parameters for xBi_2O_3-(1-x)CeO_2 were taken from ref 46 (open circles).

References

33. Mazzalai, A. et al. Characterization and Fatigue of the Converse Piezoelectric Effect in PZT Films for MEMS Application, J. Microelectromech. Syst. **24**, 831-838, (2015).

34. a) Freund, L. B., Flora, J. A. & Chason, E. Extensions of the Stoney formula for substrate curvature to configurations with thin substrates or large deformations. *Appl. Phys. Lett*. **74,** 1987-1989 (1999); b) Qiang, J., Jiang, B., Dong, Y., Roth, B. & Jiang, F. Extension of the Stoney formula for the incremental stress of thin films. *Appl. Phys. Lett*. **118**, 091604 (2021).

35. https://materialsproject.org/materials/mp-3196/

36. M. Morales, J. J. Roa, X. G. Capdevila, M. Segarra, S. Pinol, Mechanical properties at the nanometer scale of

GDC and YSZ used as electrolytes for solid oxide fuel cells, *Acta. Mater*. **58**, 2504-2509 (2010).

37. http://progs.coudert.name/elate/mp?query=mp-22891

38. Nguyen, C. H. et al. Probing-models for interdigitated electrode systems with ferroelectric thin films. *J. Phys. D. Appl. Phys*. **51**, (2018).

39. a) S. Vyas, R. W. Grimes, D. H. Gay, A. L. Rohl, Structure, stability and morphology of stoichiometric ceria crystallites, *J. Chem. Soc*., *Faraday Trans*. **94**, 427-434 (1998). b) H. Xu, R. K. Behera, Y. Wang, F. Ebrahimi, S. B. Sinnott, E. D. Wachsman, S. R. Phillpot, A critical assessment of interatomic potentials for ceria with applications to its elastic properties. *Solid State Ionics*. **181**, 551-556 (2010).

40. L. Minervini, and R. B. Grimes, Disorder in Pyrochlore Oxides, *J. Am. Ceram. Soc*. **83**, 1873-1878 (2000).

41. A. Kossoy, Q. Wang, R. Korobko, V. Grover, Y. Feldman, E. Wachtel, A. K. Tyagi, A. I. Frenkel, and I. Lubomirsky, Evolution of the local structure at the phase transition in CeO_2-Gd_2O_3 solid solutions, *Phy. Rev. B*. **87**, 054101 (2013).

42. C. Artini, G. A. Costa, M. Pani, A. Lausi, J. Plaisier, Structural characterization of the CeO_2/Gd_2O_3 mixed system by synchrotron X-ray diffraction, *J. Solid State Chem*. **190**, 24-28 (2012).

43. P. D. Battle, C. R. A. Catlow, and L. M. Moroney, Structural and dynamical studies of δ-Bi2O3 oxide-ion conductors II. A structural comparison of $(Bi_2O_3)_{1-x}$-$(M_2O_3)_x$ for M = Y, Er, and Yb, *J. Solid. State Chem.* **67**, 42-50 (1987).

44. Z. K. Heiba, M. B. Mohamed, H. Fuess, Effect of Mn doping on structural and magnetic susceptibility of C-type rare earth nano oxides $Er_{2-x}Mn_xO_3$, *Mater. Res. Bull*. **47**, 4278-4282 (2012).

45. B. Begemann, M. Jansen, Bi_4O_7, das erste definierte binÄre Bismut(III, V)-oxid, *J. Less Comm. Metal*. **156**, 123-135 (1989).

46. K. Sardar, H. Y. Playford, R. J. Darton, E. R. Barney, A. C. Hannon, D. Tompsett, J. Fisher, R. Kashtiban, J. Sloan, S. Ramos, G. Cibin, and R. I. Walton, Nanocrystalline Cerium-Bismuth Oxides: Synthesis, Structural Characterization, and Redox Properties, *Chem. Mater*. **22**, 6191-6201 (2010).